Journal of Nanobiotechnology

RESEARCH Open Access

Promotion of NLRP3 autophagosome degradation by PV-K nanodevice for protection against macrophage pyroptosis-mediated lung injury

Yan Fan[1,2], Jian Mei[3], Yuehao Shen[1], Ying Gao[1], Lina Zhao[1], Shuqi Meng[1,2], Shuai Zhou[1], Yu Qian[1], Ying Zhang[1], Zhiwei Wang[1,2], Yu Song[1], Jianfeng Liu[1,2], Shuaijie Pei[1,2], Yan Cui[5*], Hong Yang[4*], Shan-Yu Fung[3*] and Keliang Xie[1,2*]

Abstract

Acute respiratory distress syndrome (ARDS) has emerged as a significant global health challenge, with no definitive curative treatment available. Recent evidence suggests that pyroptosis of immune cells plays a pivotal role in the pathogenesis of ARDS. Targeting and modulating immune cell pyroptosis in lung tissue may offer a promising strategy to mitigate the harmful inflammation associated with this condition. In this study, we designed and synthesized a novel class of peptide-functionalized nanoparticles, PV-K, which possess an intrinsic capacity for phagocytosis by macrophages. Concurrently, the incorporation of two FFD functional groups into a single polypeptide enhances the biological activity of PV-K. Amazingly, PV-K demonstrated potent inhibitory effects on nucleotide-binding domain, leucine-rich repeat, and pyrin domain-containing protein 3 (NLRP3)-mediated pyroptosis in both mouse bone marrow-derived macrophages and the human THP-1 cell-derived macrophages. In both lipopolysaccharide and cecal ligation and puncture induced acute lung injury mouse models, treatment with PV-K significantly reduced disease severity by alleviating pulmonary inflammation and inhibiting macrophage pyroptosis. Transcriptomic analysis revealed that PV-K enhanced SQSM1/p62-mediated autophagy through upregulation of the NRF2 signaling pathway. Mechanistically, PV-K facilitated the interaction between SQSTM1/p62 and NLRP3, promoting the autolysosomal degradation of NLRP3. Notably, the inhibitory effect of PV-K on macrophage pyroptosis during acute lung injury was abrogated in *Nrf2*$^{-/-}$ mice. This study introduces a novel

The original online version of this article has been revised: Shan-Yu Fung, Hong Yang and Yan Cui should have been denoted as a corresponding author.

*Correspondence:
Yan Cui
cuiyanbio45@163.com
Hong Yang
hongyang@tmu.edu.cn
Shan-Yu Fung
shanefung@tmu.edu.cn
Keliang Xie
mzk2011@126.com

Full list of author information is available at the end of the article

nanotherapeutic approach aiming at regulating macrophage pyroptosis by facilitating NLRP3 degradation, thereby controlling inflammation in ARDS/ALI. This strategy may complement existing clinical treatments for ARDS/ALI.

Keywords NLRP3, Macrophage, Nanoparticles, Autophagosome, ALI/ARDS

Introduction

Acute respiratory distress syndrome (ARDS) and its less severe counterpart, acute lung injury (ALI), represent life-threatening conditions characterized by acute inflammation in the lungs. These conditions lead to a severe systemic inflammatory response and pose significant clinical challenges [1]. The incidence of ARDS remains alarmingly high, with mortality rates ranging from 30 to 50%, particularly in intensive care settings [2, 3]. While current treatment modalities, such as mechanical ventilation and corticosteroid therapy, can be effective, they are often accompanied by complications and limitations. This underscores the urgent need for the exploration of novel therapeutic strategies.

ARDS is marked by complex pathophysiological processes involving various cell types and signaling pathways. Recent studies have highlighted the role of the NLRP3 (NOD-like receptor family pyrin domain containing 3) inflammasome in the pathogenesis of ARDS. NLRP3 activation requires two signals: the first signal is triggered by endogenous or exogenous stimuli, leading to NF-κB-mediated upregulation of NLRP3 expression; the second signal involves cellular changes, such as potassium efflux and reactive oxygen species (ROS) generation, which promote inflammasome assembly [4–7]. The overactivation of NLRP3 contributes to a heightened inflammatory response, exacerbating lung injury and leading to severe complications in ARDS patients. Increased levels of inflammatory cytokines can amplify tissue damage and perpetuate the cycle of inflammation and injury [8–10]. Given the pivotal role of NLRP3 in various inflammatory diseases, therapeutic strategies targeting NLRP3 are currently being explored in clinical settings [11]. However, clinical research specifically focused on ARDS remains relatively limited. Thus, targeting NLRP3 to mitigate ARDS represents a novel research direction that warrants further investigation.

Nanoparticles offer several advantages over traditional drugs [12]. They can be efficiently taken up by immune cells, enhancing their therapeutic potential [13]. Additionally, nanoparticles without drug loading have shown remarkable capacity to modulate immunity and inflammation. Our previously designed nanoparticle, P12, effectively inhibits TLR signaling and inflammation by disrupting endosomal acidification in macrophages [14]. Leveraging these advantages, we developed a novel peptide-coated gold nanoparticle, PV-K, to investigate its effects on macrophage pyroptosis in ARDS.

In this study, we first identified a correlation between elevated NLRP3-associated pyroptosis in ARDS patients and lower PaO_2/FiO_2 ratios, which indicate more severe ARDS. Additionally, we found that higher levels of pyroptosis were associated with poorer prognoses, as reflected in increased Sequential Organ Failure Assessment (SOFA) and Acute Physiology and Chronic Health Evaluation II (APACHE II) scores. This suggests that elevated pyroptosis may be a critical factor influencing the severity and outcomes of ARDS. We demonstrated that heightened pyroptosis in macrophages, particularly interstitial macrophages (IMs), exacerbates inflammation in two mouse models of ALI, as assessed by multi-color flow cytometry. Subsequently, we designed the peptide-gold nanoparticle PV-K specifically to target macrophages, confirming its inhibitory effect on macrophage pyroptosis both in vitro and in vivo. The novel activity of PV-K in promoting Nrf2-SQSTM1/p62 signaling and autophagic flux was confirmed by RNA-seq. Additionally, PV-K promotes the autolysosomal degradation of NLRP3 to alleviate pyroptosis by increasing the interaction between SQSTM1/p62 and NLRP3. Importantly, Nrf2 gene deficiency was found to reverse the therapeutic effects of PV-K on ALI by inhibiting pyroptosis. These findings underscore the potential of targeting the autolysosomal degradation of NLRP3 in macrophages as a promising therapeutic strategy for ALI.

Methods

Patients

This study was approved by the Ethics Committee of Tianjin Medical University (IRB2024-YX-242-01). Inclusion criteria for ALI/ARDS patients were: (1) $PaO_2/FiO_2 \leq 300$ mmHg; (2) respiratory failure not attributable to cardiac insufficiency or fluid overload; (3) bilateral pulmonary infiltrates on X-ray or CT; (4) age > 18 years; and (5) informed consent from the family. Exclusion criteria included: (1) Glasgow Coma Scale (GCS) score < 11; (2) hematological disorders; and (3) incomplete clinical data. Control patients from the ICU met the following criteria: (1) $PaO_2/FiO_2 > 300$ mmHg; (2) normal white blood cell count (WBC), C-reactive protein (CRP), procalcitonin (PCT), and temperature; and (3) informed consent from the patient's family. Exclusion criteria for controls were: (1) recent abdominal surgery within 48 h; (2) WBC < $4 \times 10^{\wedge 9}$/L or > $10 \times 10^{\wedge 9}$/L, or body temperature > 37.3 °C; and (3) age < 18 years. A total of 30 ALI/ARDS patients and 10 controls were included (details in Table 1).

Table 1 Demographics of study participants

	Control	ARDS	*P*
Number of subjects	10	30	
Age, year	64.20 ± 17.16	71.10 ± 11.18	0.097
Sex, Female / Male	4/6	10/20	0.492
Breathing-related indicators			
Respiration rate, bpm	23 [19, 31]	27 [24, 30]	0.150
SpO_2/FiO_2	241.98 [231.71, 328.57]	151.66 [112.50, 204.44]	< 0.001
PaO_2/FiO_2	425.02 [377.10, 462.76]	199.71 [137.10, 243.85]	< 0.0001
ARDS severity (Berlin standard) (n (%))			
Mild	N/A	15 (50.00)	
Moderate	N/A	10 (33.33)	
Severe	N/A	5 (16.67)	
Laboratory parameters (median [IQR])			
White blood cell count ($\times 10^{\wedge}9\ L^{-1}$)	15.53 [9.08, 22.80]	15.93 [10.41, 25.09]	0.595
Hemoglobin ($g\ dL^{-1}$)	80.50 [54.00, 94.00]	79.50 [72.00, 91.00]	0.617
Platelet ($\times 10^{\wedge}9\ L^{-1}$)	102.50 [53.00, 231.00]	112.50 [70.00, 171.00]	0.563
Brain Natriuretic Peptide ($pg\ mL^{-1}$)	172.00 [0.00, 1490.00]	171.50 [1.30, 534.00]	0.741
Creatinine ($mg\ dL^{-1}$)	129.00 [122.00, 207.00]	87.00 [48.00, 203.00]	0.303
AST ($IU\ L^{-1}$)	45.00 [27.00, 60.00]	39.00 [26.00, 88.00]	0.779
ALT ($IU\ L^{-1}$)	37.00 [15.00, 51.00]	33.50 [18.00, 66.00]	0.851
Prognosis			
SOFA	6 [5, 8]	6 [3, 8]	0.741
APACHE II	12 [11, 15]	16 [14, 21]	0.025

Table 2 Antibodies flow cytometry

Antibodies	Source	Identifier
CD45	BioLegend	#103,139
CD3	BioLegend	#100,205
CD19	BioLegend	#115,553
CD11b	BioLegend	#101,215
Ly6C	BioLegend	#128,025
Ly6G	BioLegend	#127,627
F4/80	BioLegend	#123,115
CD64	BioLegend	#139,305
CD11c	BioLegend	#117,333
Siglec-F	BioLegend	#155,509
MHC-II	BioLegend	#107,621
Live/dead (L/D) dyes	Invitrogen	MAN0006891
FLICA	Immunochemistry	ICT-9146

Isolation and culture of peripheral blood mononuclear cells (PBMCs)

Peripheral blood was collected and centrifuged at 400 g for 10 min. The supernatant serum was stored at – 80 °C for ELISA. The cell pellet was layered onto Ficoll-Paque Plus (Sigma, MO, USA). PBMCs were obtained by slow variable speed centrifugation at 500 g for 20 min. The collected PBMCs were resuspended in RPMI-1640 (VivaCell, Shanghai, China) containing 10% fetal bovine serum (FBS, Gibco, Grand Island, NY, USA) and spread in 12-well plates (10^6 cells $well^{-1}$) to rest for 2 h before formal experiments.

Animals and ethics

Animal studies were approved by the Institutional Animal Care and Use Committee of Tianjin Medical University (IRB2024-DWFL-590). Eight-week-old adult male C57BL/6J wild-type mice (SPF Biotechnology Co., Ltd, Beijing, China) were used to establish LPS and cecal ligation and puncture (CLP)-induced ALI mouse models. *Nlrp3*$^{-/-}$ and *Nrf2*$^{-/-}$ mice were gifts from Professor Hong Yang. Mice were anesthetized with 2.5% 3-bromoethanol. The direct lung injury model was established by administrating LPS (10 mg kg^{-1}, Sigma, Aldrich, Sant-Louis, MO, USA) via intratracheal (i.t.) installation. The model of lung injury due to systemic inflammation was induced by CLP as described previously [15]. PV-K (500 nM, 50 µl, i.t.) was given 2 h before the mice perform LPS and CLP. At 24 h after LPS and CLP challenges, lung tissues, BALF, and serum were collected for further analysis.

For survival study, mice were treated with PV-K (500 nM, 50 µl, i.t.) 2 h prior to LPS (20 mg kg^{-1}, i.t.) administration. In another independent experiment, PV-K (500 nM, 500 µl) was administered intraperitoneally (i.p.) 1 day before CLP and then every 48 h in the same manner for a total of four doses. The survival of mice was monitored every 6 h for 7 days. Mouse survival and body weight changes over time were recorded and presented as Kaplan-Meier curves.

Synthesis and characterization of the peptide-coated gold nanoparticles PV-K

The synthesis of gold nanoparticles (GNP) and PV-K was conducted in accordance with previously established experimental methods [14]. Specifically, PV-K was prepared by mixing one volume of the DFFKCDFFD peptide stock solution (1 mM) with ten volumes of the GNP solution at room temperature for 24 h. Unbound peptide ligands were removed by centrifugation (14,000 rpm, 30 min, 4 °C) with PBS.

The GNPs and PV-K were visualized for their size and morphology using transmission electron microscopy (TEM) (HT7700, Hitachi, Tokyo, Japan) at an accelerating voltage of 80 kV. Their hydrodynamic diameter was determined using dynamic light scattering (DLS) on a Zetasizer (Nano ZS, Malvern, Worcestershire, UK). Zeta potential measurements were also performed on the same instrument for nanoparticles demonstrating stability. The physiological stability of GNPs and PV-K was

evaluated in 0.9% NaCl solution over various time points by monitoring the optical absorption of mono-dispersed GNPs at 524 nm. A reduction in the optical density (OD) signified nanoparticle instability.

Histological lung injury and wet/dry (W/D) ratio

The left lung lobe was stained with hematoxylin and eosin (H&E). Scoring characteristics and methods were performed according to previous studies [16]. Two experienced researchers scored each animal at eight random fields of view at 200X magnification in a double-blind manner. The W/D weight ratio of lung tissue was calculated by weighing the lung tissue before and after drying (65 °C for 48 h).

Bronchoalveolar lavage fluid (BALF) collection and staining

After anesthesia, pre-cooled saline (0.5 mL) was injected into the trachea and the procedure was repeated two more times to collect BALF. The collected BALF was centrifuged at 500 g for 8 min at 4 °C. The supernatant was collected and stored at -80 °C for cytokines, and cell precipitates were counted after resuspension in PBS. Sixty thousand cells (total volume 60 µl) were centrifuged onto slides using a cell centrifuge applicator (Thermo Fisher Scientific, Waltham, MA, USA) and stained with Liu's stain (Solarbio, Beijing, China). Five random areas on the slide were imaged, and the number of total cells, and neutrophils were counted.

Flow cytometry

After 24 h of ALI, lung tissue from the mice was digested with deoxyribonuclease I and collagenase IV to obtain single-cell suspensions. The single-cell suspensions were then separated using 40% and 80% Percoll solutions to isolate immune cells. The obtained immune cells were then stained with a variety of fluorescent antibodies and reactive dyes. Antibody information is given in Supplementary Table S1. Stained cells were detected using BD LSRFortessa flow cytometry (BD, Franklin Lake, New Jersey, USA) and data were analyzed using FlowJo software (FlowJo, LLC).

Cell culture and induction of NLRP3-associated pyroptosis

The human monocytic cell line THP-1 was cultured in complete RPMI 1640 medium supplemented with 10% FBS, 2 mM L-glutamine (Solarbio, Beijing, China), and 1 mM sodium pyruvate (Solarbio, Beijing, China). THP-1 cells were differentiated into macrophages by stimulation with 50 ng mL^{-1} phorbol myristete acetate (Sigma, Sant-Louis, MO, USA) for 24 h. Then, the cells were washed three times with PBS and rested for 48 h before experiments.

BMDMs were isolated as described previously [17]. Briefly, bone marrow cells were collected in the tibia of mice. The collected cells were cultured in IMDM complete medium (VivaCell, Shanghai, China) containing 20% L929 cell supernatant for 7 days, and 10 mL of fresh medium was added on day 3.

For pyroptosis induction, BMDMs, THP-1-derived macrophages, or PBMCs were treated with LPS (100 ng mL^{-1}) for 4 h with or without PV-K (100 nM) treatment, followed by ATP (5 mM, Sigma-Aldrich, Louis, Missouri, USA) for 30 min.

Western blot

Mouse lung tissues, PBMCs, BMDMs and THP-1-derived macrophages were lysed in RIPA buffer with a phosphatase inhibitor cocktail (Beyotime, Shanghai, China). The protein samples were first separated by SDS-PAGE electrophoresis and then transferred onto a polyvinylidene fluoride (PVDF) membrane (Millipore, Billerica, MA, USA). After blocking nonspecific binding with 5% BSA for 1 h, the membrane was incubated with primary antibodies against NLRP3, Cleaved-Caspase-1, GSDMD, Nrf2, SQSTM1/p62, and β-actin overnight at 4 °C. The next day, HRP-conjugated anti-rabbit or anti-mouse secondary antibodies were incubated for 1 h at room temperature. Finally, visualization of the protein bands was achieved by adding a chemiluminescence method (ECL, Millipore, Billerica, MA, USA) on a ChemiDoc MP imaging system (Bio-Rad, Hercules, CA, USA).

Co-immunoprecipitation

Cells were harvested and lysed in NP-40 buffer (Solarbio, Beijing, China) with a protease inhibitor cocktail. Protein concentrations were quantified using the Bradford assay. For each immunoprecipitation (IP), 500 µg of total protein was incubated with 2 µg of primary antibody specific to the NLRP3, SQSTM1/p62, or an isotype-matched control antibody overnight at 4 °C with gentle rotation. Protein A/G magnetic beads (40 µl) were added to the lysates and incubated for an additional 3 h at 4 °C. Beads-proteins complexes were washed to remove nonspecific binding and then eluted by boiling in 2× SDS sample buffer for 5 min. The interaction of NLRP3 and SQSTM1/p62 was analyzed by SDS-PAGE and Western blot.

Overexpression of NLRP3 in BMDMs

Cells were transduced with a lentiviral vector encoding mouse *Nlrp3* or a control vector (Genechem, Shanghai, China). BMDMs were infected with the lentivirus in the presence of HitransG P. After 24 h, the medium was replaced with fresh complete IMEM containing 20% L929 cell supernatant, and the cells were cultured for an additional 72 h to allow for stable expression of NLRP3. Overexpression of NLRP3 was confirmed via EGFP expression and Western blot analysis.

Fluorescence co-localization by confocal microscope

After the intervention, cells were fixed with 4% paraformaldehyde (Solarbio, Beijing, China) for 10 min and permeabilized with 0.3% Triton X-100 (Solarbio, Beijing, China) for 10 min. Cell samples were incubated overnight at 4 °C with Rabbit-NLRP3 and Mouse-SQSTM1/p62 primary antibodies. The following day, Goat Anti-Mouse-Alexa Fluor® 488 and Goat Anti-Rabbit-Alexa Fluor® 647 were added and incubated at room temperature for 1 h. Nuclei were then stained using Hoechst 33,258 (Solarbio, Beijing, China) for 10 min. Fluorescence co-localization images were acquired using a confocal microscope (LSM800, Leica, Wetzlar, Hessen, Germany). Pearson's R value was calculated using ImageJ software.

Internalization and Subcellular distribution of PV-K in BMDMs

BMDMs were seeded in confocal dishes and co-incubated with Cy5-labelled PV-K for 4 h. Then, BMDMs were stained for cell membranes with DiO (10 μM, Solarbio, Beijing, China) for 20 min at 37 °C. Finally, the nuclei were stained with Hoechst 33,258 for 10 min at room temperature. Imaging was performed using confocal microscopy (LSM800, Leica, Wetzlar, Hessen, Germany).

Transmission electron microscopy (TEM) was employed to examine the subcellular localization of the PV-K nanoparticles. BMDMs (8×10^6 cells/well) were cultured in 10-cm plates and exposed to PV-K at a concentration of 100 nM for 4 h. The harvested cells were transferred to microcentrifuge tubes and fixed with 2.5% glutaraldehyde in PBS on ice for 2 h. The fixed samples were subsequently processed by the Sevier Experimental Center and imaged using an HT7800 TEM (Hitachi, Tokyo, Japan) at an accelerating voltage of 80 kV.

Autophagy flux by confocal imaging

THP-1 cells expressing the RFP-GFP-LC3B fusion protein (InvivoGen, Carlsbad, California, France) were used to detect autophagic flux. These cells express human LC3B (microtubule-associated protein 1 light chain 3 β) fused to two fluorescent reporter proteins: RFP (acid-stable) and GFP (acid-sensitive) [18, 19]. When autophagosomes are formed, there is progressive degradation of GFP and a simultaneous increase in RFP signal. The ratio of RFP to GFP in cells is used to assess autophagic flux. Cells were differentiated into macrophages and then treated with LPS and ATP. Then, cells were imaged by confocal microscopy (LSM800, Leica, Wetzlar, Hessen, Germany). The ratio of RFP and GFP were counted using ImageJ in three separate independent experiments.

Cell death counting using Propidium Iodide (PI) staining

After treatment, BMDMs and THP-1-derived macrophages were stained with diluted PI (Beyotime, Shanghai, China) for 15 min in an incubator (Thermo, Waltham, Massachusetts, USA) at 37 °C and 5% CO_2. Finally, cells (at least 5 fields of view per well) were imaged under a fluorescence microscope (Olympus, Tokyo, Japan) at a magnification of 400×. The PI-DNA complexes exhibited excitation and emission wavelengths of 535 nm and 615 nm, respectively. Cell morphology was imaged using light microscopy. Channel merging and counting were performed using ImageJ. At least three independent experiments were conducted.

Quantitative real-time qPCR

Total RNA was extracted from tissue samples or cells by homogenization with TRIzol reagent (Invitrogen, Carlsbad, California, USA) and converted to cDNA using Evo M-MLV Reverse Transcription Reagent Premix (Accurate Biology, Changsha, China). Quantitative real-time PCR was performed using primers for Nlrp3, Ccaspase-1, IL-1β, and IL-18 (specific sequences detailed in Supplementary Table S2Table 3We would like to place Table3 in the Supplementary material and name it Supplementary Table S2. Please help me to modify it, thank you very much.). Relative mRNA expression was quantified using the $2^{(-\Delta\Delta Ct)}$ method

mRNA-Sequencing (RNA-seq) and data analysis

Total RNA of BMDMs was extracted using TRIzol reagent. RNA purity and concentration were evaluated using the NanoDrop 2000 spectrophotometer (Thermo Scientific, Waltham, Massachusetts, USA). Transcriptome sequencing and analysis were conducted by OE Biotech Co., Ltd. (Shanghai, China).

The libraries were sequenced on an illumina Novaseq 6000 platform and principal component analysis (PCA) was performed using R (v 3.2.0) to evaluate the biological duplication of samples. Differential expression analysis was performed using the DESeq2. An adjust p-value < 0.05 and $|\log2FC| > 1.5$ were set as the thresholds for significantly differential expression gene (DEGs). Among the DEGs, $\log2FC > 0$ represents up-regulated genes while $\log2FC < 0$ represents down-regulated genes. Heatmaps of clustering of different genes between groups and Venn diagrams comparing different groups using OECloud tool (https://cloud.oebiotech.com). WikiPathways enrichment analysis and Gene Set Enrichment Analysis (GSEA) of DEGs was drawn based on the R (https://www.r-project.org/) on the OECloud platform (https://cloud.oebiotech.com/task/).

Statistical analysis

All statistical tests were performed with Prism 9.4.1 software (GraphPad Software). Student t-test was employed for the comparison between two groups, and one-way analysis of variance (ANOVA) was used for pairwise

comparison among multiple comparisons. Experiments were repeated at least three times as independent experiments. P-value of <0.05 was considered statistically significant.

Results

Increased NLRP3-associated pyroptosis in ARDS patients

The role of NLRP3-related pyroptosis was assessed using PBMCs, serum, and BALF samples from ARDS patients and controls (Fig. 1A; Table 1). Immunoblotting revealed increased expression of NLRP3 and GSDMD-N in PBMCs from the ARDS patients compared with the controls (Fig. 1B). ELISA further confirmed that the levels of NLRP3 protein in PBMCs and IL-1β in serum were both higher in ARDS patients than those in the controls (Fig. 1C), with a positive correlation between them (Fig. 1D). Patients with elevated NLRP3 and IL-1β levels exhibited reduced PaO_2/FiO_2 levels, indicative of more

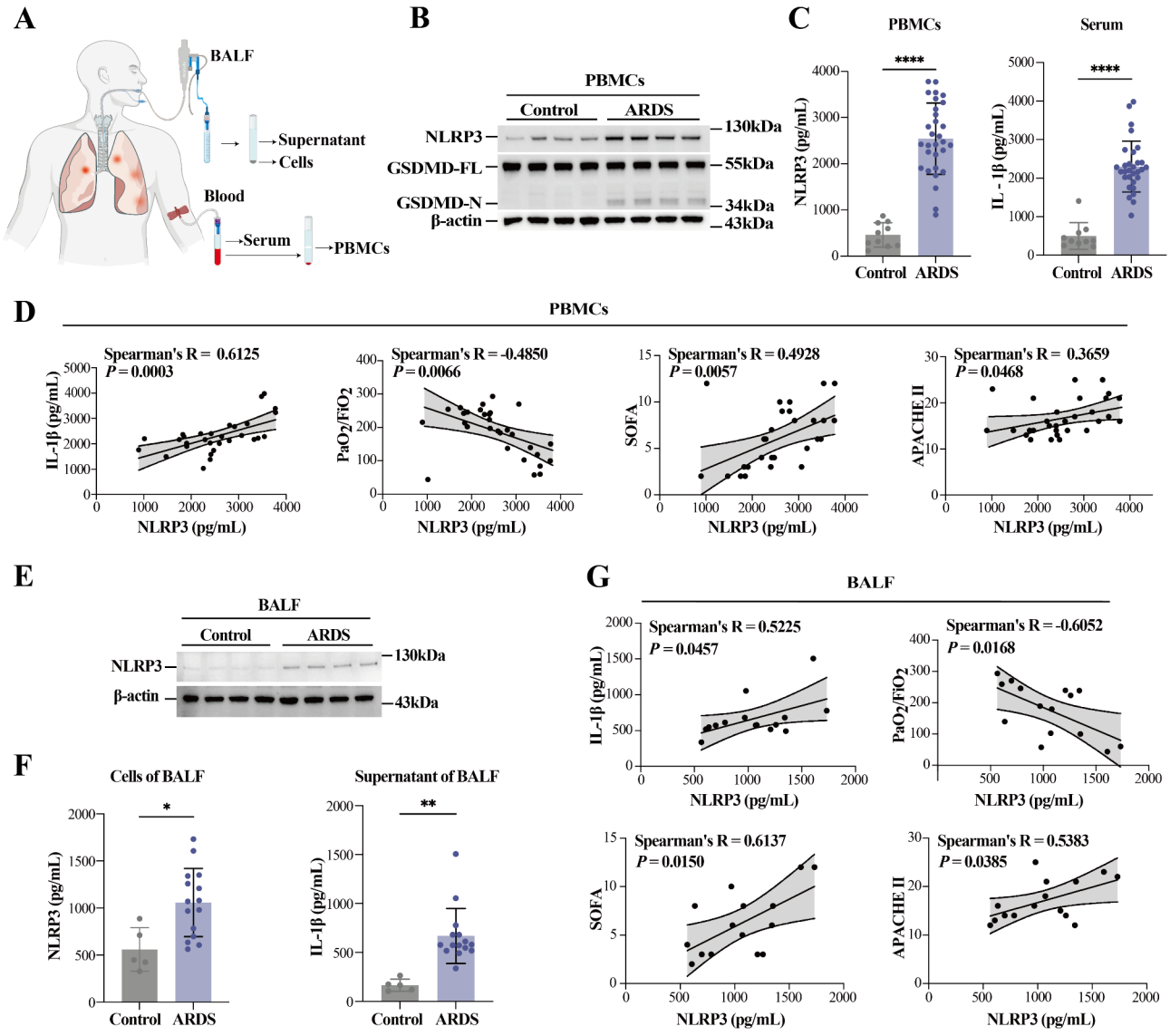

Fig. 1 Increased NLRP3-associated pyroptosis in ARDS patients. **(A)** Peripheral blood mononuclear cells (PBMCs) and bronchoalveolar lavage fluid (BALF) samples were collected from patients with acute respiratory distress syndrome (ARDS) and controls. **(B)** Immunoblot analysis showing NLRP3 and GSDMD-N protein levels in PBMCs from ARDS patients compared with the controls. **(C)** ELISA results indicate NLRP3 levels in PBMCs and IL-1β levels in serum from ARDS patients and controls. **(D)** The correlation of NLRP3 expression in PBMCs with IL-1β, PaO_2/FiO_2 ratio, SOFA score, and APACHE II score is demonstrated (**B**: Control, $n=6$; ARDS, $n=6$; **C** and **D**: Control, $n=10$; ARDS, $n=30$). **(E)** Immunoblot analysis shows NLRP3 expression levels in BALF from ARDS patients compared to controls. **(F)** ELISA results show NLRP3 levels in BALF and IL-1β levels in the supernatant from ARDS patients and controls. **(G)** The correlation of NLRP3 expression in BALF with IL-1β, PaO_2/FiO_2 ratio, SOFA score, and APACHE II score is presented (**E**: Control, $n=4$; ARDS, $n=6$; **F** and **G**: Control, $n=5$; ARDS, $n=15$). *P* values were calculated using an unpaired t test; $^*P<0.05$, $^{**}P<0.01$, $^{***}P<0.001$, and $^{****}P<0.0001$. Pearson's correlation coefficient (r) is indicated

Table 3 Sequences of real-time qPCR

Primer	Forward sequences	Reverse sequences
Nlrp3	AGCCTTCCAGGATCCTCTTC	CTTGGGCAGCAGTTTCTTTC
Caspase–1	AGATGGCACATTTCCAGGAC	GATCCTCCAGCAGCAACTTC
IL-1β	GAAATGCCACCTTTTGACAGTG	TGGATGCTCTCATCAGGACAG
IL-18	AAGACTCTTGCGTCAACTTCAAGGA	AGTCGGCCAAAGTTGTCTGATTC
GAPDH	CATCACTGCCACCCAGAAGACTG	ATGCCAGTGAGCTTCCCGTTCAG

severe ARDS, along with elevated SOFA and APACHE II scores. (Fig. 1D, Supplementary Fig. 1A). NLRP3 was also elevated in BALF cells from ARDS patients, correlating with higher IL-1β levels in the supernatant (Fig. 1E, F, G). This increases was also negatively correlated with PaO_2/FiO_2 and positively with SOFA and APACHE II scores (Fig. 1G, Supplementary Fig. 1B). These findings suggest that NLRP3-driven pyroptosis is upregulated in ARDS patients, contributing to disease severity.

Enhanced pyroptosis in macrophages contributes to ALI

Given these remarkable findings, we sought to identify which immune cells predominantly undergo pyroptosis in response to lung injury. To this end, mouse models were generated, including a direct ALI model induced by LPS and a systemic ALI model induced by CLP (Fig. 2A). Multi-color flow cytometry was used to assess the pyroptosis ($Dead^+$, caspase-1^+) in B cells ($CD45^+$, $CD19^+$), T cells ($CD45^+$, $CD3^+$), Neutrophils ($CD11b^+$, $Ly6G^+$), Macrophages ($CD11b^+$, $Ly6G^-$, $F4/80^+$), and Monocytes ($CD11b^+$, $Ly6G^-$, $Ly6C^+$) (Fig. 2B). The incidence of pyroptosis in macrophages and monocytes was found to be elevated in the LPS group in comparison to the PBS group (Fig. 2C). A similar trend was observed in the CLP model, where an increase in pyroptosis levels was noted in macrophages (Fig. 2D). Lung macrophages include alveolar macrophages (AMs) and interstitial macrophages (IMs) (Figure S2). While no significant difference in pyroptosis levels was observed in AMs ($CD64^+$, $CD11C^+$, MHC $II^±$, Siglec F^+), IMs ($CD64^+$, $CD11C^+$, MHC II^+, Siglec F^-) exhibited significantly increased pyroptosis levels in the both LPS and CLP groups (Fig. 2E, F). A reduction in macrophages, coupled with an increase in neutrophils in BALF from patients with ARDS compared to controls, may be a contributing factor to pyroptosis (Fig. 2G, H). In summary, these findings underscore the critical role of macrophage pyroptosis in the pathogenesis of ALI.

PV-K, a macrophage-targeting hybrid, attenuates NLRP3-dependent pyroptosis in macrophages

Considering the therapeutic potential of the previously studied P12, we designed a novel hybrid, PV-K, synthesized from gold nanoparticles (GNPs) and V-type peptides (Fig. 3A). Physicochemical analysis showed that PV-K nanoparticles maintained a predominant spherical morphology comparable with the bare GNPs, exhibiting predominantly spherical structures as observed under TEM (Fig. 3B). Dynamic light scattering (DLS) confirmed that PV-K had a larger hydrodynamic diameter than bare GNPs, indicating successful peptide conjugation (Fig. 3C). The zeta potential of both GNPs and PV-K was approximately − 40 mV, indicating that the nanoparticles had sufficient stability (Fig. 3D). The stability of PV-K was evaluated by measuring the absorbance of the mono-dispersed GNPs at 524 nm. The results demonstrated that PV-K remained stable in 0.9% NaCl solution over time (up to 24 h), whereas the bare GNPs became unstable immediately (Fig. 3E). Further confirmation of PV-K stability was obtained through DLS measurements, which showed that the hydrodynamic diameter of PV-K in 0.9% NaCI solution remained consistent at 19.45 ± 0.09 nm (PDI: 0.17 ± 0.01), 18.20 ± 0.07 nm (PDI: 0.18 ± 0.01), 17.99 ± 0.08 nm (PDI: 0.18 ± 0.01), and 18.14 ± 0.11 nm (PDI: 0.18 ± 0.00) at 0 h, 1 h, 12 h, and 24 h, respectively (Fig. 3F). Moreover, confocal microscopy confirmed PV-K-Cy5 uptake by macrophages (Fig. 3G). Additionally, subcellular localization of PV-K was examined using TEM, which revealed that PV-K primarily accumulated within endosomes or lysosomes (Fig. 3H).

PV-K was then tested for its ability to mitigate NLRP3-mediated pyroptosis in macrophages. In BMDMs, PV-K alone had no effect, but it significantly reduced pyroptosis and IL-1β levels in the presence of LPS and ATP (Fig. 3I-K). Furthermore, the upregulation of NLRP3, GSDMD-N, and Cleaved-Caspase-1 proteins induced by LPS + ATP stimulation was diminished by PV-K treatment (PV-K + LPS + ATP) (Fig. 3L). Consistent results were observed in THP-1 induced macrophages, where PV-K treatment (PV-K + LPS + ATP) similarly reduced pyroptosis, supernatant IL-1β levels, and key pyroptotic proteins (Fig. 3M-P). Collectively, these outcomes indicate that the novel hybrid PV-K effectively inhibits NLRP3-related pyroptosis by targeting macrophages.

PV-K rescued ALI in vivo through reduction of NLRP3-mediated macrophage pyroptosis

The in vivo therapeutic efficacy of the PV-K was evaluated in an LPS-induced ALI model (Figure S3A). Mice subjected to PBS + LPS exhibited only 20% survival at 7 days, whereas PV-K pre-treatment improved survival to 70% (Fig. 4A). Additionally, PV-K treatment reduced neutrophil counts, total cell numbers, and protein concentrations in BALF compared to PBS + LPS (Fig. 4B, Figure S3B). Lung injury scores were lower in the PV-K + LPS group, particularly in terms of reduced neutrophil infiltration (Fig. 4C, Figure S3C). PV-K also

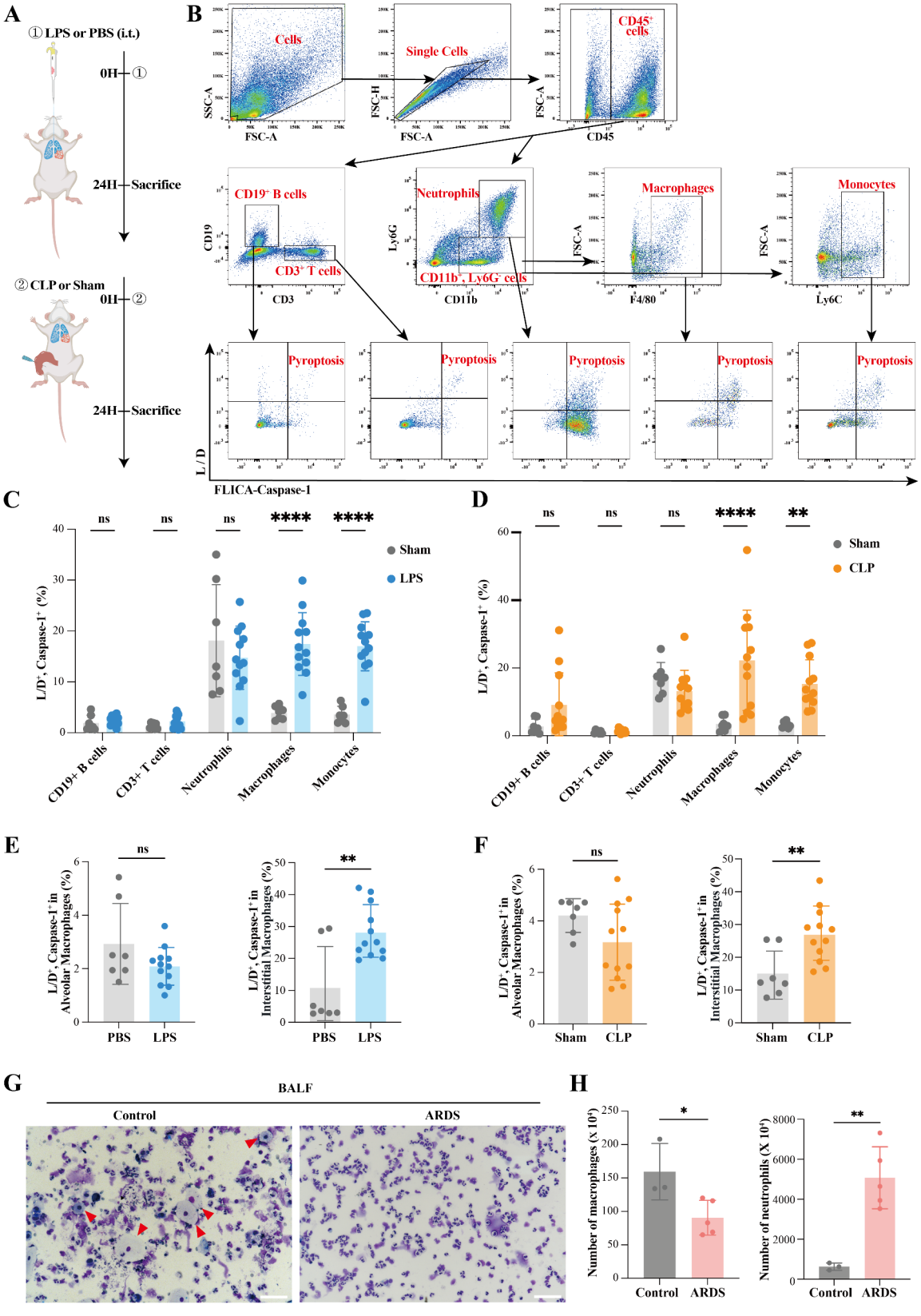

Fig. 2 (See legend on next page.)

(See figure on previous page.)

Fig. 2 Enhanced pyroptosis in macrophages contributes to ALI. **(A)** Experimental procedures for the intratracheal (i.t.) administration of LPS (10 mg kg^{-1}) to induce direct ALI model and CLP induced system ALI model. **(B)** Gating strategy employed in the multi-color flow cytometer. **C** and **D**. Percent of pyroptosis (L/D^+, Caspase-1^+ cells) of immune cells in LPS- and CLP- induced ALI models. **E** and **F**. Percent of pyroptosis (L/D^+, Caspase-1^+ cells) of alveolar macrophages (AMs) and interstitial macrophages (IMs) in LPS- and CLP- induced ALI model (**C-F**: PBS or Sham, $n = 7$; LPS or CLP, $n = 12$). **G**. Images of the BALF cells collected from ARDS patients and controls. Scale bar, 100 μm. **H.** Quantification of macrophage (left) and neutrophil (right) counts in the BALF (Control, $n = 3$; ARDS, $n = 5$). *P* values were calculated using an unpaired t-test; ns = not significant, $^*P < 0.05$, $^{**}P < 0.01$, $^{***}P < 0.001$, and $^{****}P < 0.0001$

inhibited LPS-induced upregulation of NLRP3, Cleaved-Caspase-1, and GSDMD-N (Fig. 4D). Pyroptosis ($Dead^+$, Caspase-1^+) in macrophages ($CD11b^+$, $Ly6G^-$, $F4/80^+$) were notably reduced by PV-K (Fig. 4E), indicating anti-inflammatory effects and inhibition of macrophage pyroptosis in LPS-induced ALI.

In a CLP-induced ALI model (Figure S3D), PV-K treatment (PV-K + CLP) reduced neutrophil infiltration in BALF, lung histopathological inflammation, and inhibited NLRP3, Cleaved-Caspase-1, and GSDMD-N expression (Fig. 4F-H, S3E-F). Pyroptosis in macrophages was similarly reduced in PV-K + CLP group than PBS + CLP (Fig. 4I). PV-K treatment (PV-K + CLP) improved survival rates from 10 to 30% at day 7 (Fig. 4J). These results suggest that PV-K effectively reduces in vivo inflammation by inhibiting macrophage pyroptosis.

PV-K induces Nrf2-SQSTM1/p62 signaling activation and autophagic flux

The impact of PV-K on macrophage pyroptosis-related gene expression and signaling pathways was investigated via RNA sequencing (RNA-seq) of differentially expressed genes (DEGs) in the Unstimulated, LPS + ATP and PV-K + LPS + ATP groups, with notable changes observed in the PV-K + LPS + ATP group compared to LPS + ATP (Fig. 5A). Venn diagram analysis revealed that PV-K treatment up-regulated the expression of 374 genes previously down-regulated by LPS + ATP (Fig. 5B). WikiPathways analysis indicated significant enrichment of the Nrf2 signaling pathway among these genes (Fig. 5C). Gene Set Enrichment Analysis (GSEA) further demonstrated that PV-K treatment up-regulated the Nrf2 signaling pathway (Fig. 5D). Moreover, the transcript level of SQSTM1/p62 was increased, ranking among the top 10 up-regulated genes in the Nrf2 pathway upon PV-K treatment (Fig. 5E). Western blotting confirmed that the expression levels of Nrf2 and SQSTM1/p62 proteins was elevated in the PV-K treatment group (PV-K + LPS + ATP) compared to LPS + ATP (Fig. 5F).

To assess the effects of PV-K treatment on autophagic flux, THP1-Difluo™ hLC3 reporter cells were utilized. Confocal imaging revealed that PV-K treatment (PV-K + LPS + ATP) enhanced the RFP/GFP ratio, suggesting an increase in autophagosomal degradation of cargo (Fig. 5G, H). In summary, these findings indicate that PV-K promotes cargo degradation via activation of the Nrf2-SQSTM1/p62 pathway and heightened autophagic flux, particularly in the context of NLRP3 inflammasome activity.

PV-K enhances the interaction between NLRP3 and SQSTM1/p62 to promote NLRP3 degradation

It is well-established that NLRP3 inflammasome activation involves both initiation and activation steps [20]. Following the receipt of an initiating signal, such as LPS, NLRP3 expression is increased. Subsequently, active signals, like ATP and nigericin, trigger the assembly of the NLRP3 inflammasome [21, 22]. In the initial signal, BMDMs were stimulated with LPS for 4 h, revealing that the PV-K + LPS treatment did not reduce NLRP3 protein expression compared to LPS alone (Fig. 6A). qPCR analysis further confirmed that PV-K treatment (PV-K + LPS + ATP) did not diminish *Nlrp3* transcription levels induced by the initial signal (Fig. 6B). Thus, we hypothesized that PV-K mediates NLRP3 degradation. To test this hypothesis, we evaluated NLRP3 stability in BMDMs using the protein synthesis pan-inhibitor cycloheximide (CHX), which demonstrated that PV-K treatment (PV-K + LPS + ATP) enhanced NLRP3 degradation (Fig. 6C, D). Next, the proteasome inhibitor MG132, the early autophagy inhibitor 3-MA and the autophagy lysosome inhibitor CQ were applied to elucidate the degradation pathway of NLRP3, and it was found that autophagosomes serve as the primary pathway for NLRP3 degradation facilitated by PV-K (Fig. 6E, F).

Given that SQSTM1/p62 is a key selective autophagy receptor and that substrate-bound SQSTM1/p62 is degraded by lysosomes, we posited that NLRP3 might be a substrate for SQSTM1/p62. Confocal images and co-immunoprecipitation confirmed that the interaction between SQSTM1/p62 and NLRP3 was enhanced following PV-K treatment (Fig. 6G-I). Following NLRP3 overexpression, the inhibitory effect of PV-K on NLRP3 and GSDMD-N expression was diminished (Fig. 6J). Notably, the reduction in NLRP3 and GSDMD-N achieved through PV-K treatment mirrored that seen in *Nlrp3*$^{-/-}$ mice (Fig. 6K). In conclusion, PV-K primarily exerts its therapeutic effect by promoting NLRP3 degradation.

Nrf2 decreases the NLRP3-dependent pyroptosis to protect against ALI

Nrf2 knockout mice were used to investigate whether the therapeutic effect of PV-K on ALI remains effective. In wild-type (WT) mice, PV-K treatment rescued 30%

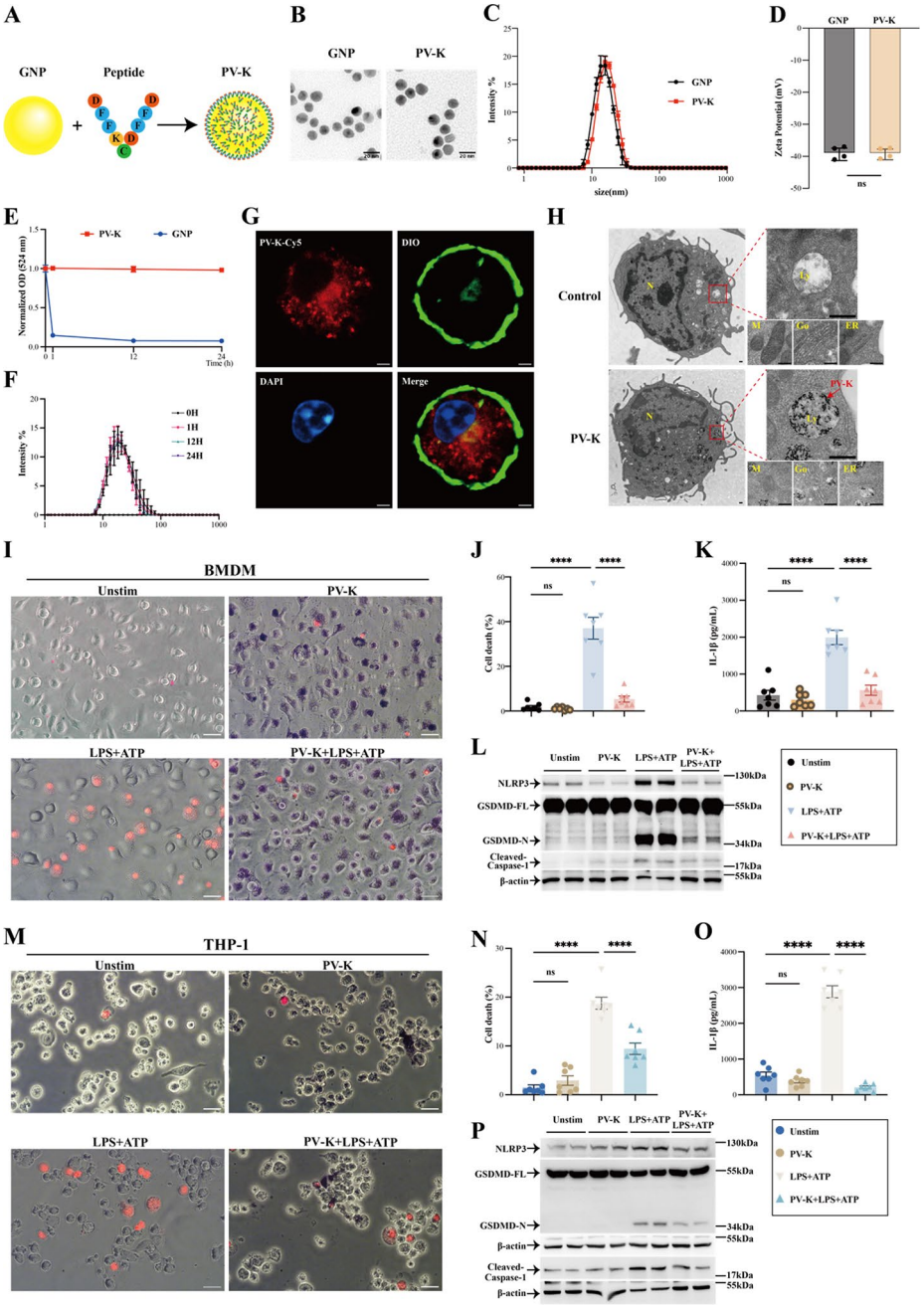

Fig. 3 PV-K, a macrophage-targeting hybrid, attenuates NLRP3-dependent pyroptosis in macrophages. **(A)** Schematic illustration depicting the synthesis process of the peptide-coated gold nanoparticle PV-K. **(B)** The TEM images showing the morphology of the bare GNPs and PV-K; scale bar = 20 nm.**(C)** DLS was used to analyze the intensity based hydrodynamic size profiles of the bare GNPs and PV-K. **(D)** Measurements of zeta potential for both bare GNPs and PV-K. **(E)** Absorbance (at 524 nm) of the bare GNPs and PV-K in 0.9% NaCl solution over time (0-24 h). **(F)** The time-dependent physiological stability of the PV-K was assessed by DLS analysis the hydrodynamic diameter profiles of PV-K in 0.9% NaCl solution at 0 h, 1 h, 12 h, and 24 h. **(G)** Confocal images of macrophages treated with PV-K-Cy5 for 4 h with the cell membrane stained with DiO (green) and the nuclei stained with DAPI (blue); scale bar: 5 μm. **(H)** TEM images showing the subcellular localization of PV-K in the endosomal vesicles and lysosomes (Ly) in BMDM; cells were treated with PV-K (100 nM) for 4 h; red arrows indicated the internalized nanoparticles; Scale bar = 200 nm. N: nucleus, Ly: lysosome, M: mitochondrion, Go: Golgi complex, ER: endoplasmic reticulum. **I-L.** Propidium Iodide (PI) staining images (**I**), quantification of cell death (**J**), levels of IL-1β in the culture supernatant (**K**) and immunoblot analysis (**L**) in BMDMs stimulated by LPS + ATP with the presence or absence of PV-K. (**I-K**: $n = 7$; **L**: $n = 6$). **M-P.** PI staning images (**M**), quantification of cell death (**N**), levels of IL-1β in the culture supernatant (**O**) and immunoblot analysis (**P**) of THP-1 cell-derived macrophages stimulated with LPS + ATP in the presence or absence of PV-K. (**M-O**: $n = 7$; **P**: $n = 6$). LPS: 100 ng mL^{-1} for 4 h; ATP: 5 mM for 30 min after LPS; PV-K: 100 nM for 4.5 h. *P* values were calculated using unpaired t-test; ns = not significant, $^{**}P < 0.01$, and $^{****}P < 0.0001$

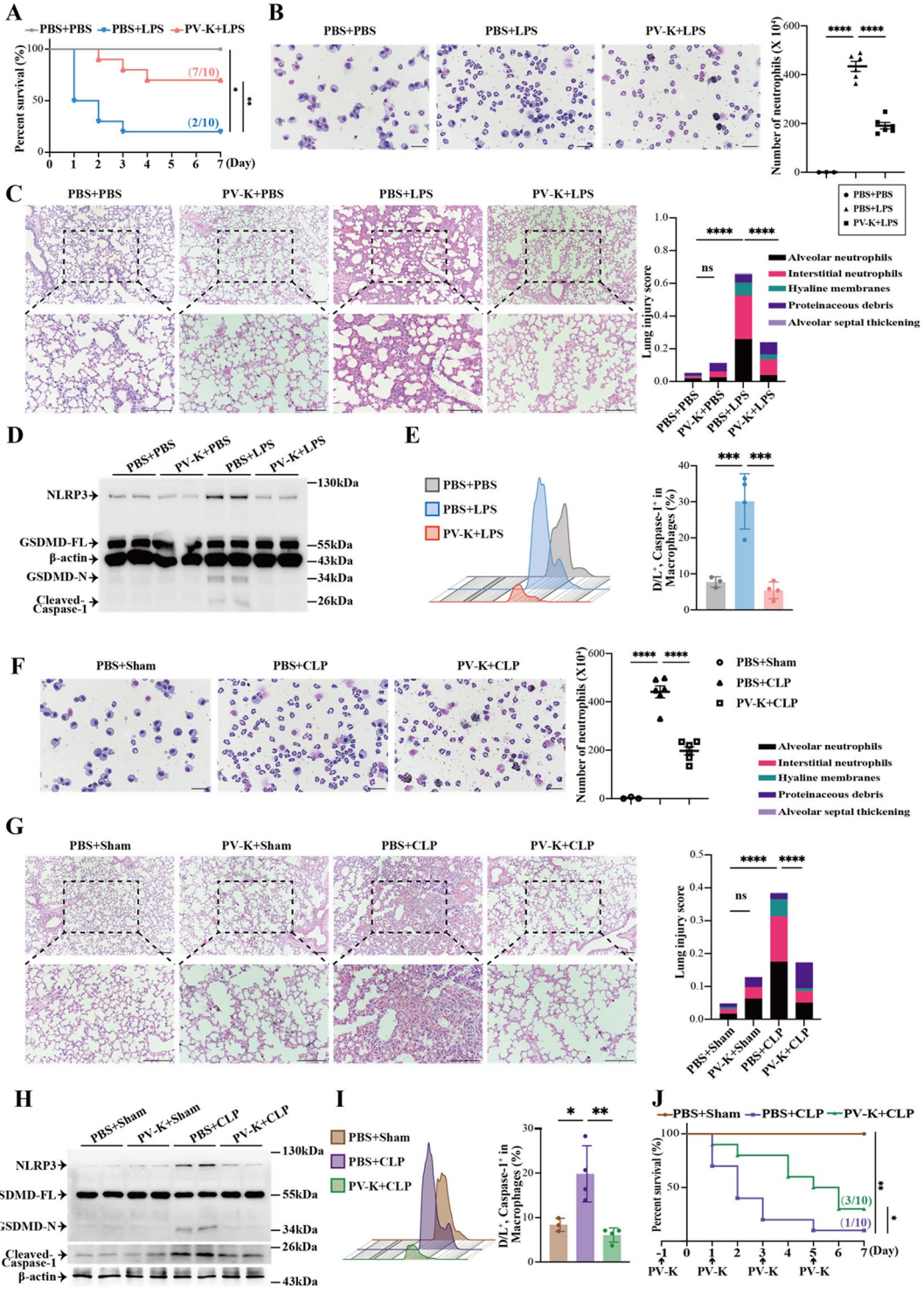

Fig. 4 PV-K rescued ALI in vivo through reduction of NLRP3-mediated macrophage pyroptosis. **A-E.** The therapeutic effect of PV-K in LPS-induced ALI model. Survival rates (**A**), BALF images and neutrophil counts (**B**), histological images and total lung injury score of H&E-stained lung sections (**C**), immunoblot analysis of lung tissues (**D**), and percentages of pyroptotic macrophages (**E**) in the lungs after PV-K treatment compared to the LPS group. **F-J.** The effective effect of PV-K in the CLP-induced ALI model. BALF images and neutrophil counts (**F**), histological images and total lung injury score of H&E-stained lung sections (**G**), immunoblot analysis of lung tissues (**H**), percentages of pyroptotic macrophages (**I**), and survival rates (**J**) upon PV-K treatment compared to the CLP group. In the survival study (**A**), mice received a single intratracheal injection of LPS (20 mg kg^{-1}). For the other analyses (**B-E**), LPS (10 mg kg^{-1}, i.t., 24 h) was used. PV-K (500 nM, i.t.) before 2 h of LPS or CLP (**A-I**). For the CLP survival study (**J**), PV-K (500 nM, i.p.) was administered 24 h before CLP and then at 48-hour intervals. $n > 3$ per group. P values were calculated using one-way ANOVA; $^{*}P < 0.05$, $^{**}P < 0.01$, $^{***}P < 0.001$, and $^{****}P < 0.0001$

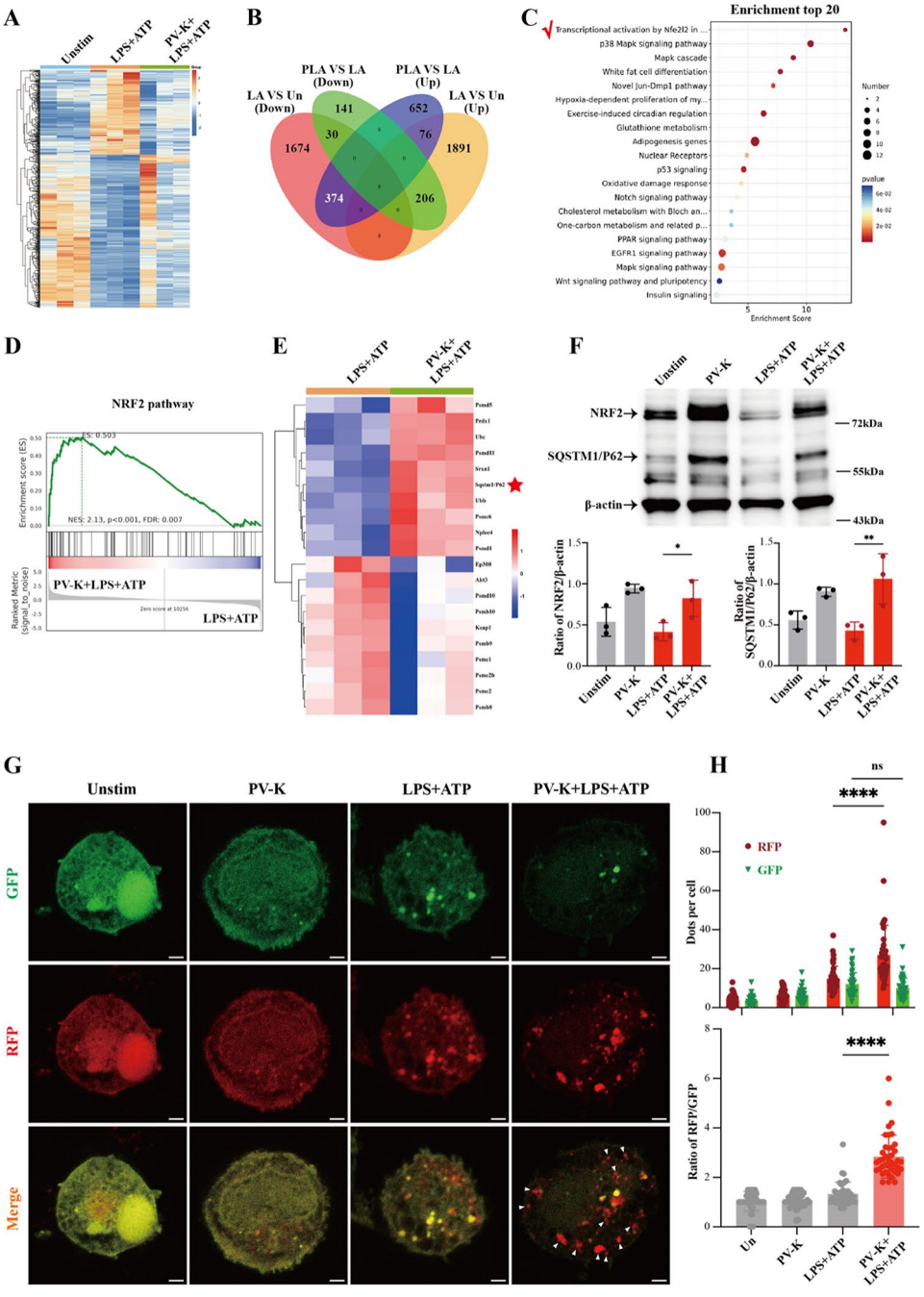

Fig. 5 PV-K induces Nrf2-SQSTM1/p62 signaling activation and autophagic flux. **(A)** Heatmap showing the expression profiles of three study groups: Unstimulated (Unstim), LPS + ATP, and PV-K + LPS + ATP. Thresholds were set at $P < 0.05$ and log2(fold change) > 1.5. **(B)** Venn diagrams illustrating the overlap of up-regulated and down-regulated genes between two of the three groups. LA VS Un (down): down-regulation in LPS + ATP compared to the Unstim group. PLA VS LA (down): down-regulation in PV-K + LPS + ATP compared to the LPS + ATP group. LA VS Un (up): up-regulation in LPS + ATP compared to the Unstim group. PLA VS LA (up): up-regulation in PV-K + LPS + ATP compared to the LPS + ATP group. **(C)** Bubble plots showing the top 20 Wikipathway enrichment analysis of genes at the intersection of PLA VS LA (up) and LA VS Un (down). **(D)** GSEA analysis of Nrf2 signaling pathway in the PV-K + LPS + ATP and LPS + ATP groups. **(E)** Cluster map of the top 10 genes based on GSEA analysis of Nrf2 signaling pathway in the PV-K + LPS + ATP and LPS + ATP groups. **(F)** Immunoblot analysis (up) and statistical analysis (down) of Nrf2, SQSTM1/p62, and β-actin in BMDMs from four groups: Unstim, PV-K, LPS + ATP, and PV-K + LPS + ATP. **(G)** Confocal images of the THP-1 cells expressing the RFP-GFP-LC3 fusion protein treated in Unstim, PV-K, LPS + ATP, and PV-K + LPS + ATP groups. Scale bar: 5 μm. **(H)** Evaluation of RFP and GFP dots per cell and RFP/GFP ratio in each group. Forty cells were observed in each group. LPS: 100 ng mL^{-1} for 4 h; ATP: 5 mM for 30 min after LPS; PV-K: 100 nM for 4.5 h. *P* values were calculated using one-way ANOVA; ns = not significant, $^{*}P < 0.05$, $^{**}P < 0.01$, and $^{****}P < 0.0001$

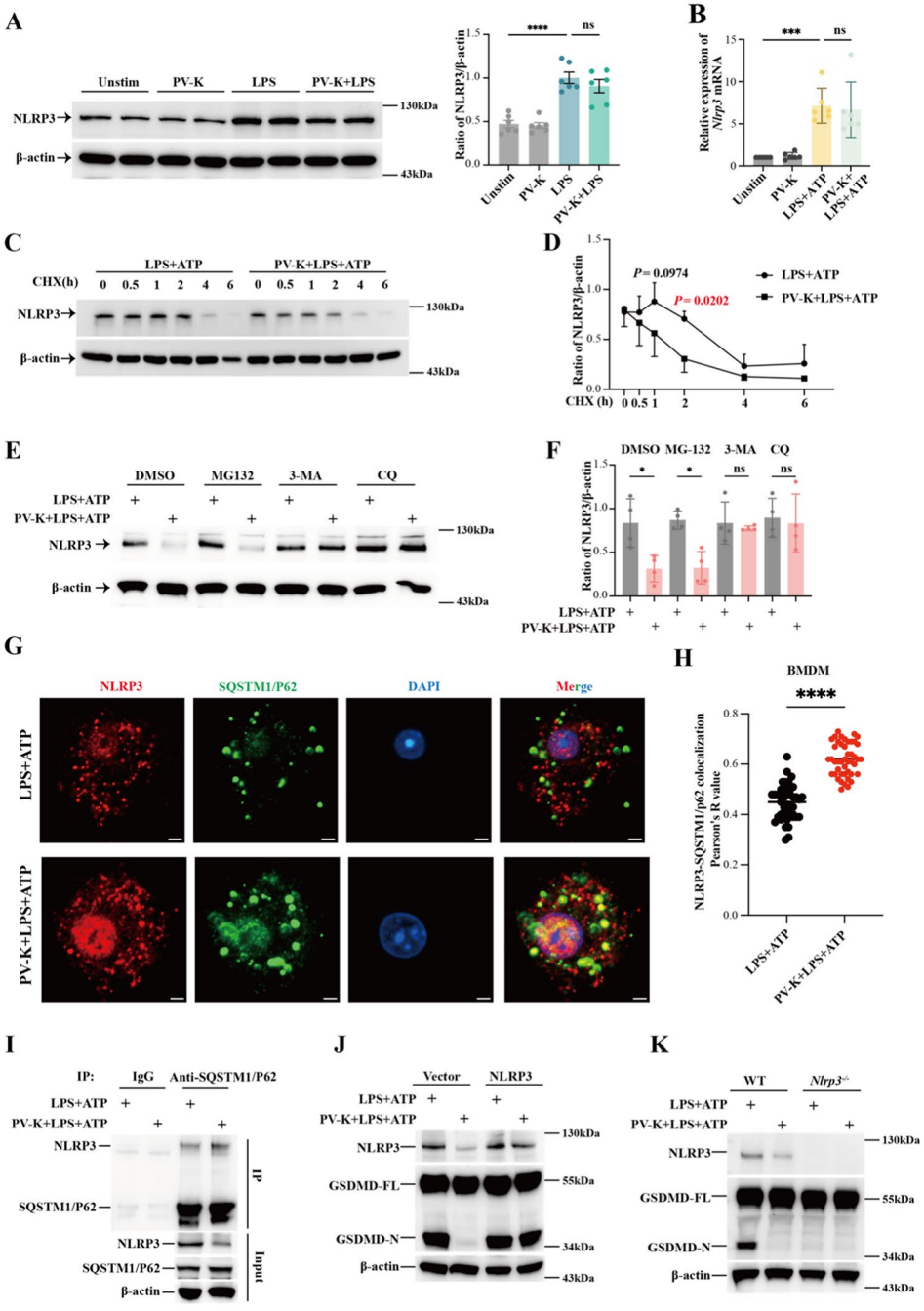

Fig. 6 PV-K enhances the interaction between NLRP3 and SQSTM1/p62 to promote NLRP3 degradation. **(A)** Immunoblot analysis (left) and quantification (right) of NLRP3 protein levels in BMDMs stimulated with LPS (100 ng mL^{-1}) with the presence or absence of PV-K (100 nM). **(B)** Relative expression of *Nlrp3* mRNA in BMDMs stimulated with LPS (100 ng mL-1) with or without PV-K (100 nM) for 4 h, followed by ATP (5 mM) for 30 min. **C-D.** The BMDMs pre-treated with cycloheximide (CHX, 100 μM) were subsequently stimulated with LPS (100 ng mL^{-1}) with or without PV-K (100 nM) for 4 h, followed by ATP (5 mM) for 30 min. Immunoblot analysis (**C**) and statistical analysis (**D**) of the NLRP3 expressions were performed at different time points. **E-F.** BMDMs were pre-treated with MG132 (20 μM), 3-MA (5 μM), or CQ (30 μM) for 2 h, followed by stimulation with LPS (100 ng mL^{-1}) with or without PV-K (100 nM) for 4 h, and then ATP (5 mM) for 30 min. Immunoblot analysis (**E**) and quantification (**F**) of NLRP3 expressions were conducted. **G.** Confocal images showing the localization of NLRP3 (Red), SQSTM1/p62 (Green), and DAPI (Blue) in BMDMs stimulated with LPS (100 ng mL^{-1}) with or without PV-K (100 nM) for 4 h, followed by ATP (5 mM) for 30 min. Scale bar: 5 μm. $n = 45$ cells per group. **H.** Evaluation of Pearson's R value in each cell. **I.** Co-immunoprecipitation analysis showing the interaction between NLRP3 and SQSTM1/p62. **J.** Immunoblot analysis showing the therapeutic effect of PV-K after lentiviral overexpression of *Nlrp3*. **K.** Immunoblot analysis showing the therapeutic effect of PV-K in WT and *Nlrp3*$^{-/-}$ BMDMs. $n > 3$. At least three independent experiments were performed. *P* values were calculated using one-way ANOVA; ns = not significant, $^{*}P < 0.05$, $^{***}P < 0.001$, and $^{****}P < 0.0001$

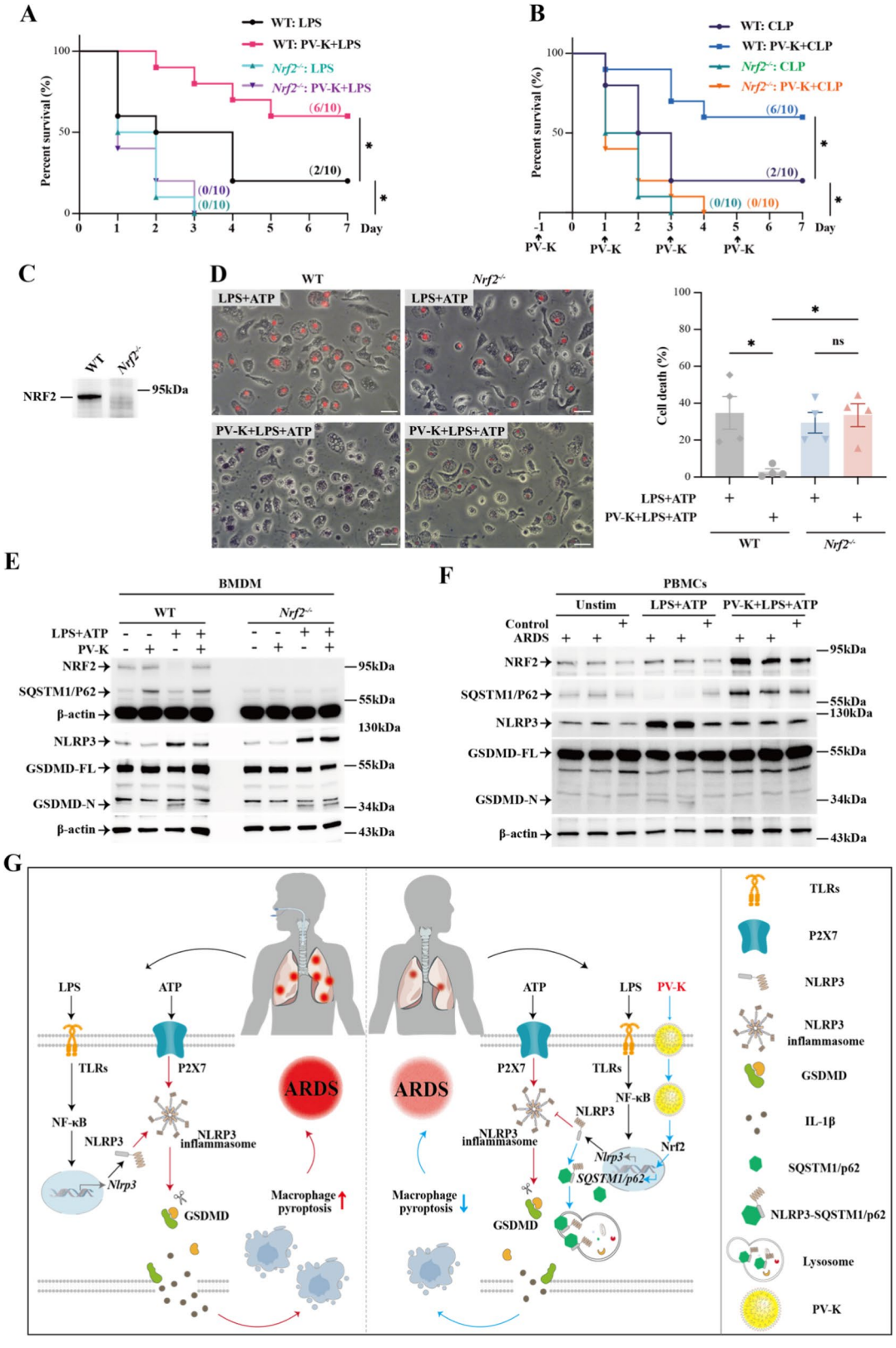

Fig. 7 (See legend on next page.)

(See figure on previous page.)

Fig. 7 NRF2 decreases the NLRP3-dependent pyroptosis to protect against ALI. **(A)** Survival rates of WT and *Nrf2*$^{-/-}$ mice pre-treated with PV-K (500 nM) for 2 h and then challenged with LPS (20 mg kg^{-1}). $n = 10$. **(B)** Survival rates of WT and *Nrf2*$^{-/-}$ mice administered PV-K (500 nM, i.p.) 24 h before CLP, followed by additional doses at 48-hour intervals. $n = 10$. **(C)** Immunoblot analysis of NRF2 expression levels in WT and *Nrf2*$^{-/-}$ BMDMs. **(D)** PI staning images and quantification of pyroptosis in WT and *Nrf2*$^{-/-}$ BMDMs stimulated by LPS + ATP with the presence or absence of PV-K. $n = 4$. **(E)** Immunoblot analysis of NRF2, SQSTM1/p62, NLRP3, GSDMD-FL, GSDMD-N, and β-actin levels in WT and *Nrf2*$^{-/-}$ BMDMs stimulated with LPS + ATP with or without PV-K (100 nM). $n = 4$. **(F)** Immunoblot analysis of NRF2, SQSTM1/p62, NLRP3, GSDMD-FL, GSDMD-N, and β-actin levels in PBMCs from ARDS patients and control patients. (Control, $n = 3$; ARDS, $n = 6$). **(G)** Summary diagram illustrating macrophages pyroptosis in ARDS and the therapeutic role of PV-K. *P* values were calculated using one-way ANOVA; ns = not significant, $^{*}P < 0.05$

of mouse survival upon LPS stimulation, but this protective effect was absent in *Nrf2*$^{-/-}$ mice, and *Nrf2*$^{-/-}$ mice showed a diminished capacity to resist LPS stimulation (Fig. 7A). Similar results were observed in the CLP-induced ALI model, where *Nrf2*$^{-/-}$ mice did not respond to PV-K treatment and diminished resistance to stress (Fig. 7B). In *Nrf2*$^{-/-}$ BMDMs, reduced Nrf2 expression was confirmed, accompanied by a decrease in SQSTM1/p62 (Fig. 7C, E). While PV-K inhibited pyroptosis in WT BMDMs under LPS + ATP stimulation, this effect was absent in *Nrf2*$^{-/-}$ BMDMs (Fig. 7D), and the suppression of NLRP3 and GSDMD-N by PV-K was lost in *Nrf2*$^{-/-}$ BMDMs (Fig. 7E). In PBMCs from patients, PV-K increased the expression of Nrf2 and SQSTM1/p62 while concurrently inhibiting NLRP3 and GSDMD-N (Fig. 7F). Collectively, these results imply that PV-K's protective effects against ALI are mediated by the activation of Nrf2-SQSTM1/p62 signaling and NLRP3 degradation, supporting its potential for clinical applications.

Discussion

Pyroptosis, a form of programmed cell death, plays a crucial role in activating the body's inflammatory and immune responses. However, excessive pyroptosis can lead to harmful, exaggerated inflammation [4, 5, 22]. The overactivation of the NLRP3 inflammasome is a key factor in ALI and ARDS [8, 9]. For example, Pan's research demonstrated that SARS-CoV-2 N protein interacts with NLRP3, enhancing its activation and driving excessive inflammation [9]. This highlights the significant role of NLRP3 in ALI/ARDS, although most of these findings come from preclinical studies. Our study, involving 30 ARDS patients and 10 ICU controls, showed elevated NLRP3 levels in ARDS patients, especially those with severe ARDS ($PaO_2/FiO_2 < 100$). Higher NLRP3 expression correlated with greater organ failure and worse long-term outcomes (higher SOFA and APACHE II scores). These results offer a foundation for understanding ARDS pathophysiology, though further research with larger cohorts is needed.

Previous studies have established that autophagic regulation of NLRP3 is significant [23]. Under low inflammation, AMP-activated protein kinase (AMPK) activation and inhibition of mTOR signaling promote autophagy-related gene expression and degradation. Conversely, uncontrolled inflammation depletes autophagy-related proteins, impairing NLRP3 degradation and increasing pyroptosis [24]. In this study, PV-K-mediated autophagy was a protective autophagy under the stimulation of pyroptosis activation. On the one hand, PV-K promoted the timely increase of SQSTM1/p62 through the activation of Nrf2, thereby complementing its degradation. On the other hand, PV-K enhanced the increased interaction between SQSTM1/p62 and NLRP3 to promote the autolysosomal degradation of NLRP3.

Existing studies have shown that Nrf2 can promote the transcription and expression of SQSTM1/p62 [25]. Possible mechanisms are as follows: First, SQSTM1/p62 is a ubiquitin-binding protein known to bind competitively to KEAP1 for autophagic degradation. KEAP1 degradation releases its binding partner, the antioxidant transcription factor Nrf2, from the Nrf2-Keap1 complex and leads to nuclear activation of Nrf2, which promotes SQSTM1/p62 expression [26]. Second, nuclear translocation of transcription factor EB (TFEB) activates Nrf2, which in turn promotes SQSTM1/p62-dependent selective autophagy. In this case, PV-K promoted the activation of the Nrf2-SQSTM1/p62 signaling pathway, which may be related to both mechanisms.

In ALI/ARDS, increased lung permeability allows for passive targeted delivery of nanoparticles [27]. Nanomedicine offers advantages in addressing the limitations of traditional anti-inflammatory and antioxidant therapies [28, 29]. Key features of nanotherapeutics include: (1) Targeted delivery to lung cells through passive, active, or physicochemical modifications, reducing toxicity and enhancing efficacy [30, 31]; (2) The use of nanocarriers to deliver various therapeutic agents [32]; (3) The ability to increase the dose of treatment at target organs while minimizing side effects [32]. Here, we developed a novel peptide-gold hybrid, PV-K, targeting macrophages. Intratracheal administration of PV-K effectively suppressed inflammation in ALI/ARDS by inhibiting NLRP3-mediated pyroptosis, even without additional therapeutic agents.

Conclusion

In summary, increased NLRP3-associated pyroptosis was found to be correlate with lower PaO_2/FiO_2 ratios and worse prognosis in ARDS. Furthermore, pyroptosis predominantly occurred in macrophages rather than in other immune cells response lung injury. To enhance

macrophage targeting, we designed and applied the peptide nanoparticle PV-K. The ability of PV-K to inhibit pyroptosis was validated both in vitro and in mouse models of ALI. This inhibitory effect was primarily achieved through the activation of the Nrf2-SQSTM1/p62 signaling pathway, which promotes the autophagy-lysosomal degradation of NLRP3. This study presents a potential therapeutic strategy for ARDS facilitating the degradation of NLRP3 in macrophages. Additionally, it underscores the rapid translation of nanomedicine to complement the current clinical treatments of ARDS.

Abbreviations

ARDS	Acute respiratory distress syndrome
NLRP3	Nucleotide-binding domain, leucine-rich repeat, and pyrin domain-containing protein 3
SOFA	Sequential Organ Failure Assessment
APACHE II	Acute Physiology and Chronic Health Evaluation II
PBMCs	Peripheral blood mononuclear cells
BALF	Bronchoalveolar lavage fluid
LPS	Lipopolysaccharide
CLP	Cecal ligation and puncture

Supplementary Information

The online version contains supplementary material available at https://doi.org/10.1186/s12951-025-03219-y .

Supplementary Material 1

Acknowledgements

We thank Dr. Hefan Zhang and Rui Zhang from the Laboratory of Immunology of Tianjin Medical University for their help in the experiment. We also express our gratitude to the Scientific Research Sharing Platform of Tianjin Medical University and the faculty for their help.

Author contributions

Y. F. and J. M. wrote the main manuscript text. Y. S., Y. G., L. Z., S. M. and S. Z. designed the work. Y. Q., Y. Z., Z. W., Y. S., J. L. and S. P. analysis. Y. C. revised the manuscript. H. Y., S. F. and K. X. reviewed the manuscript.

Funding

This work was supported by Tianjin Medical University General Hospital Clinical Research Program (22ZYYLCCG05 for Keliang Xie), China International Medical Foundation (2021-N-15 for Keliang Xie), the National Natural Science Foundation of China (No. 82270096 and 82470080 for HY; 81971549 for SYF), the Natural Science Foundation of Tianjin Municipal Science and Technology Commission (21CYBJC01650 for SYF), and Tianjin Municipal Education Commission Key Natural Science Project (2023ZD012 for HY).

Data availability

No datasets were generated or analysed during the current study.

Declarations

Ethics approval and consent to participate

This study involving human participants were approved by the Ethics Committee of Tianjin Medical University (IRB2024-YX-242-01). Additionally, all animal procedures were authorized by the Institutional Animal Care and Use Committee of Tianjin Medical University (IRB2024-DWFL-590).

Consent for publication

Not applicable.

Competing interests

The authors declare no competing interests.

Author details

[1]Department of Critical Care Medicine, Tianjin Medical University General Hospital, No. 154, Anshan Road, Heping District, Tianjin 300052, China
[2]Department of Anesthesiology, Tianjin Institute of Anesthesiology, Tianjin Medical University General Hospital, Tianjin 300052, China
[3]State Key Laboratory of Experimental Hematology, Key Laboratory of Immune Microenvironment and Disease (Ministry of Education), Department of Immunology, School of Basic Medical Science, International Joint Laboratory of Ocular Diseases, Ministry of Education, Tianjin Medical University, Tianjin 300070, China
[4]Department of Pharmacology and Tianjin Key Laboratory of Inflammation Biology, School of Basic Medical Sciences, Intensive Care Unit of the Second Hospital, The Province and Ministry Co-Sponsored Collaborative Innovation Center for Medical Epigenetics, Tianjin Medical University, Tianjin 300070, China
[5]Department of Pathogen Biology, School of Basic Medical Sciences, Tianjin Medical University, Tianjin 300070, China

Received: 2 November 2024 / Accepted: 10 February 2025
Published online: 27 February 2025

References

1. Gorman EA, O'Kane CM, McAuley DF. Acute respiratory distress syndrome in adults: diagnosis, outcomes, long-term sequelae, and management. Lancet. 2022;400:1157–70.
2. Matthay MA, Arabi Y, Arroliga AC, et al. A New Global Definition of Acute Respiratory Distress Syndrome. Am J Respir Crit Care Med. 2024;209:37–47.
3. Bellani G, Laffey JG, Pham T, et al. Epidemiology, patterns of Care, and mortality for patients with Acute Respiratory Distress Syndrome in Intensive Care Units in 50 countries. JAMA. 2016;315:788–800.
4. Gross O, Thomas CJ, Guarda G, et al. The inflammasome: an integrated view. Immunol Rev. 2011;243:136–51.
5. Strowig T, Henao-Mejia J, Elinav E, et al. Inflammasomes in health and disease. Nature. 2012;481:278–86.
6. Schroder K, Zhou R, Tschopp J. The NLRP3 inflammasome: a sensor for metabolic. Danger? Sci. 2010;327:296–300.
7. Broz P, Dixit VM. Inflammasomes: mechanism of assembly, regulation and signalling. Nat Rev Immunol. 2016;16:407–20.
8. Xian H, Liu Y, Rundberg Nilsson A, et al. Metformin inhibition of mitochondrial ATP and DNA synthesis abrogates NLRP3 inflammasome activation and pulmonary inflammation. Immunity. 2021;54:1463–e7711.
9. Pan P, Shen M, Yu Z, et al. SARS-CoV-2 N protein promotes NLRP3 inflammasome activation to induce hyperinflammation. Nat Commun. 2021;12:4664.
10. Wang Y, Liu Y, Liu Q, et al. Caspase-1-Dependent pyroptosis of Peripheral Blood mononuclear cells is Associated with the severity and mortality of septic patients. Biomed Res Int. 2020;2020:9152140.
11. Vora SM, Lieberman J, Wu H. Inflammasome activation at the crux of severe COVID-19. Nat Rev Immunol. 2021;21:694–703.
12. Dos Santos Haupenthal DP, Mendes C, de Bem Silveira G, et al. Effects of treatment with gold nanoparticles in a model of acute pulmonary inflammation induced by lipopolysaccharide. J Biomed Mater Res A. 2020;108:103–15.
13. Getts DR, Shea LD, Miller SD, et al. Harnessing nanoparticles for immune modulation. Trends Immunol. 2015;36:419–27.
14. Sun L, Liu Y, Liu X, et al. Nano-enabled reposition of Proton Pump inhibitors for TLR inhibition: toward a new targeted nanotherapy for Acute Lung Injury. Adv Sci (Weinh). 2022;9:e2104051.
15. Hubbard WJ, Choudhry M, Schwacha MG, et al. Cecal ligation and puncture. Shock. 2005;24(Suppl 1):52–7.
16. Matute-Bello G, Downey G, Moore BB, et al. An official American Thoracic Society workshop report: features and measurements of experimental acute lung injury in animals. Am J Respir Cell Mol Biol. 2011;44:725–38.
17. Weischenfeldt J, Porse B. Bone Marrow-Derived Macrophages (BMM): Isolation and Applications. CSH Protoc 2008;2008:pdb prot5080.
18. Loos B, du Toit A, Hofmeyr JH. Defining and measuring autophagosome flux-concept and reality. Autophagy. 2014;10:2087–96.

19. Kimura S, Noda T, Yoshimori T. Dissection of the autophagosome maturation process by a novel reporter protein, tandem fluorescent-tagged LC3. Autophagy. 2007;3:452–60.
20. Xu J, Nunez G. The NLRP3 inflammasome: activation and regulation. Trends Biochem Sci. 2023;48:331–44.
21. Lamkanfi M, Dixit VM. Mechanisms and functions of inflammasomes. Cell. 2014;157:1013–22.
22. Shi J, Zhao Y, Wang K, et al. Cleavage of GSDMD by inflammatory caspases determines pyroptotic cell death. Nature. 2015;526:660–5.
23. Nakahira K, Haspel JA, Rathinam VA, et al. Autophagy proteins regulate innate immune responses by inhibiting the release of mitochondrial DNA mediated by the NALP3 inflammasome. Nat Immunol. 2011;12:222–30.
24. Puschel GP, Klauder J, Macrophages HJ. Low-Grade inflammation, Insulin Resistance and hyperinsulinemia: a mutual ambiguous relationship in the development of metabolic diseases. J Clin Med 2022;11.
25. Lu C, Xue L, Luo K, et al. Colon-accumulated gold nanoclusters alleviate intestinal inflammation and prevent secondary colorectal carcinogenesis via Nrf2-Dependent macrophage reprogramming. ACS Nano. 2023;17:18421–32.
26. Taguchi K, Fujikawa N, Komatsu M, et al. Keap1 degradation by autophagy for the maintenance of redox homeostasis. Proc Natl Acad Sci U S A. 2012;109:13561–6.
27. Qiao Q, Liu X, Yang T, et al. Nanomedicine for acute respiratory distress syndrome: the latest application, targeting strategy, and rational design. Acta Pharm Sin B. 2021;11:3060–91.
28. Sadikot RT. The potential role of nano- and micro-technology in the management of critical illnesses. Adv Drug Deliv Rev. 2014;77:27–31.
29. Dong X, Zhang CY, Jin G et al. Targeting of Nanotherapeutics to infection sites for Antimicrobial Therapy. Adv Ther (Weinh) 2019;2.
30. Wu Y, Ma J, Woods PS, et al. Selective targeting of alveolar type II respiratory epithelial cells by anti-surfactant protein-C antibody-conjugated lipoplexes. J Control Release. 2015;203:140–9.
31. Howard MD, Greineder CF, Hood ED, et al. Endothelial targeting of liposomes encapsulating SOD/catalase mimetic EUK-134 alleviates acute pulmonary inflammation. J Control Release. 2014;177:34–41.
32. Blanco E, Shen H, Ferrari M. Principles of nanoparticle design for overcoming biological barriers to drug delivery. Nat Biotechnol. 2015;33:941–51.

Publisher's note